Mott transition and collective charge pinning in electron doped Sr_2IrO_4

K. Wang,[1] N. Bachar,[1] J. Teyssier,[1] W. Luo,[1] C. W. Rischau,[1] G. Scheerer,[1] A. de la Torre,[1,2] R. S. Perry,[3] F. Baumberger,[1] and D. van der Marel[1,*]

[1]*Department of Quantum Matter Physics, University of Geneva, 24 Quai Ernest-Ansermet, 1211 Geneva 4, Switzerland*
[2]*Institute for Quantum Information and Matter, California Institute of Technology, Pasadena, California 91125, USA*
[3]*London Centre for Nanotechnology and UCL Centre for Materials Discovery, University College London, London WC1E 6BT, United Kingdom*

(Received 16 January 2018; revised manuscript received 14 May 2018; published 5 July 2018)

We studied the in-plane dynamic and static charge conductivity of electron doped Sr_2IrO_4 using optical spectroscopy and DC transport measurements. The optical conductivity indicates that the pristine material is an indirect semiconductor with a direct Mott gap of 0.55 eV. Upon substitution of 2% La per formula unit the Mott gap is suppressed except in a small fraction of the material (15%) where the gap survives, and overall the material remains insulating. Instead of a zero energy mode (or Drude peak) we observe a soft collective mode (SCM) with a broad maximum at 40 meV. Doping to 10% increases the strength of the SCM, and a zero-energy mode occurs together with metallic DC conductivity. Further increase of the La substitution doesn't change the spectral weight integral up to 3 eV. It does however result in a transfer of the SCM spectral weight to the zero-energy mode, with a corresponding reduction of the DC resistivity for all temperatures from 4 to 300 K. The presence of a zero-energy mode signals that at least part of the Fermi surface remains ungapped at low temperatures, whereas the SCM appears to be caused by pinning a collective frozen state involving part of the doped electrons.

DOI: 10.1103/PhysRevB.98.045107

I. INTRODUCTION

Doped Mott insulators have been found to exhibit a rich spectrum of remarkable physical phenomena, including metal-insulator transitions, charge and spin ordering, stripe order, orbital currents, high-T_c superconductivity, and the pseudogap phenomenon [1]. Sr_2IrO_4 has a quasi-two-dimensional structure of corner sharing IrO_6 octahedra. Due to tilting of the octahedra there are two equivalent Ir superlattices organized in a $\sqrt{2} \times \sqrt{2}$ superstructure in the plane. The combination of tetragonal crystal field and spin-orbit interaction makes that for each of the Ir atoms two of the $5d$ bands are well below the Fermi energy E_F and are therefore fully occupied, one band cuts the Fermi surface and is half full, and the two remaining $5d$ bands are far above E_F and therefore empty. The on-site Coulomb energy further splits the half-filled band in a filled lower Hubbard band (LHB) and an empty upper Hubbard band (UHB). Doping this Hubbard insulator results in a strongly correlated metal. It has been suggested that this material can be turned into a high T_c superconductor [2]. While antiferromagnetism and spin density wave order have been reported for different doping concentrations [3–5], up to date transport and magnetization data have not revealed superconductivity [3,6]. A recent angle resolved photoemission (ARPES) study found an anisotropic pseudogap in $Sr_{2-y}La_yIrO_4$ [6]. ARPES [7] and STM [8] experiments on K-covered Sr_2IrO_4 further reported evidence for a d-wave gap closing at 30–50 K. In addition a degeneracy splitting of the bands near $(\pi,0)$ was found in ARPES experiments [6] and a hidden order parameter has been claimed based on observations with optical second harmonic generation [9]. These observations have lead to different mutually exclusive speculations as to the nature of this state of matter, in particular superconducting fluctuations [7] and a d-wave pseudospin-current ordered state [10]. ARPES and STM probe the single electron spectral function. Information on the *collective* current response requires on the other hand measurements of the optical conductivity.

Here we use optical spectroscopy from 12.5 meV to 4 eV and DC transport experiments of pristine and doped Sr_2IrO_4 to measure the doping evolution of the free carrier density and the optical spectra. We report the following results: (i) We demonstrate the appearance of a MIR mode at 0.2 eV for all dopings, the intensity of which tracks the charge carrier concentration. This feature is common with other doped Mott systems such as the cuprates. (ii) We demonstrate that a rapid collapse of the Mott gap is obtained with doping. However, an important part of the doped carrier response shows up in a soft collective mode at finite frequencies at the detriment of the spectral weight of the Drude peak even for dopings as high as $y = 0.1$ and to a lesser extent for $y = 0.18$. (iii) We present theoretical calculations of the optical conductivity of the Mott-insulating parent compound, as well as the doped material, using the self-consistent Hartree-Fock approximation. The calculations reproduce the single-particle band structure as measured with ARPES and the doping dependence of the Drude spectral weight. However, the effects of doping at finite energy are not fully captured by this approach, thus

*dirk.vandermarel@unige.ch

TABLE I. Lanthanum doping in the chemical formula $Sr_{2-y}La_yIrO_4$ using WDS and number of conduction electrons per formula unit from the Fermi surface observed with ARPES [6].

y (WDS)	N_e (ARPES)
0	
0.02 (0.005)	
0.10 (0.02)	0.084 (0.030)
0.18 (0.04)	0.13 (0.03)

motivating the development of alternative theories for this class of materials. (iv) We determine the quasilinear doping dependence of the spectral weight of the zero-energy mode (the Drude peak), from which we obtain the kinetic energy $K^*(y)$ of the renormalized charge carriers, and show that $K^*(y)$ is approximately five times smaller than in the hole-doped cuprates. (v) Our observations point toward a scenario where the collective charge sector is composed of two components, one associated to ungapped fermions, and the other to a frozen correlated state of the electrons (for example a charge density wave) pinned by disorder associated with the donor states.

II. METHODS AND RESULTS

Single crystals of $Sr_{2-y}La_yIrO_4$ were grown as described in Appendix A. Stoichiometry and doping concentrations are reported in Table I. The complex dielectric function and optical conductivity were determined in the range of 12.5 meV to 4 eV by combining reflectivity and ellipsometry methods as described in Appendix A. The resulting low energy optical conductivity for different temperatures and dopings is displayed in Fig. 1. For the doped samples we observe a zero-energy mode (D). The zero-energy conductivity corresponds to the inverse of the DC resistivity which has been measured using standard transport methods and is shown in Fig. 2. The DC resistivity was measured on samples of the same composition, grown under identical conditions. The $y = 0.1$ and $y = 0.18$ samples approach a linear temperature dependence at high temperature and have a resistivity upturn at low temperatures (see inset of Fig. 2), whereas the resistivity of the $y = 0.0$ and $y = 0.02$ samples has a negative slope at all temperatures indicating insulating or at best bad metal behavior. The fact that the DC conductivities (full symbols in Fig. 1) and the peak maxima of the zero-energy mode do not coincide indicates that the spectrum below the measured range (20 meV for this sample) is not fully described by the Drude-Lorentz model employed here. We emphasize however, that despite the lack of detail below 20 meV, the spectral weight in this range can be obtained accurately by analyzing the real and imaginary dielectric function at higher frequencies [11]. In the range between 0 and 100 meV we observe optical phonon excitations. These modes are most prominent in the undoped compound (see Table II). Upon doping all modes exhibit Fano-type asymmetries. With the exception of the 82 meV mode, the phonons disappear against the electronic background in the samples with doping of $y = 0.1$ and $y = 0.18$, signaling an effective channel for charge screening at high doping. Upon doping $y = 0.02$ a

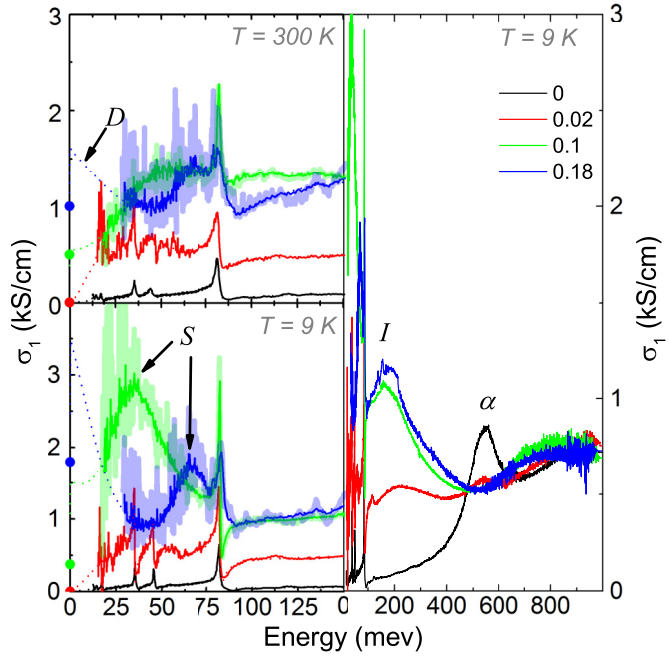

FIG. 1. Left: doping dependence of the optical conductivity from 0 to 0.15 eV at 300 K and 9 K. The dashed curves represent extrapolations of the optical conductivity obtained from fitting reflectivity $R(\omega)$ with a Drude-Lorentz parametrization. The shaded areas correspond to the noise level of the original reflectivity data (see Fig. 7). The dark lines are the result of binning the data in intervals of 0.3 meV. Full symbols correspond to the conductivity values measured in DC transport (see Fig. 2). Right: doping dependence in the range of 0 to 1 eV at 9 K.

SCM appears with a maximum at 40 meV (labeled S), which sharpens and gains spectral weight for $y = 0.1$ and collapses into the Drude peak for $y = 0.18$. For the same doping a SCM appears at 60 meV. Since the spectral weight in these modes is far too high for phonons, they have to correspond to electronic

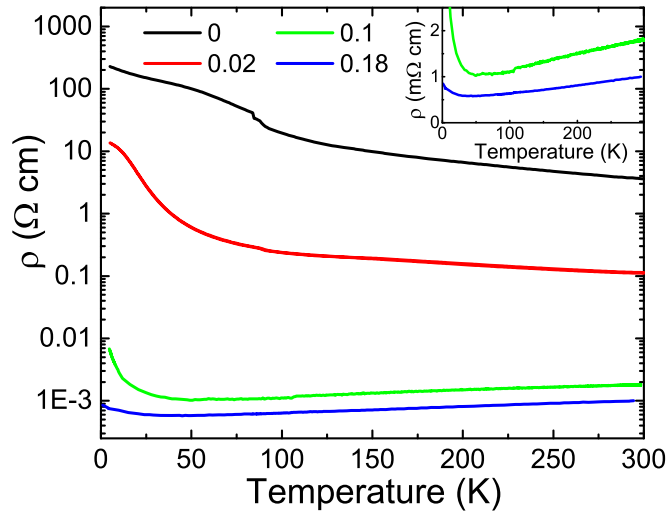

FIG. 2. Temperature dependence of the resistivity for different doping compositions.

TABLE II. Fitted parameter values for the optical phonons of the $y = 0$ sample at a temperature of 9 K.

$\hbar\omega_j$ meV	$\hbar\gamma_j$ meV	S_j	θ_j degrees	Mode	Type
12.8	0.58	1.2	0	$E_u(1)$	External
14.3	0.61	1.2	0	$E_u(2)$	External
17.1	0.33	1.4	0	$E_u(3)$	External
35.0	0.69	1.4	31	$E_u(4)$	Bending
45.5	0.88	0.7	42	$E_u(5)$	Bending
81.8	1.8	1.0	46	$E_u(6)$	Stretching

collective modes. These modes strongly couple to the optical phonons, which is strikingly demonstrated by the $E_u(4)$, $E_u(5)$, and $E_u(6)$ modes (see Table II), each overlapping with the energy of the SCM. Fano-type asymmetry has also been observed for the Raman active phonons in the doped material [12]. For the $y = 0.02$ sample it cannot be excluded that this asymmetry may—at least in part—have to do with electronic heterogeneity that we will discuss in the following section. However, since phonon asymmetry is a commonly observed and well understood consequence of electron-phonon coupling [13,14], this interpretation likely applies to all samples. The absence of the $E_u(4)$ and $E_u(5)$ phonons from the $y = 0.1$ and $y = 0.18$ spectra is probably due to strong mixing with the SCM. We notice that some asymmetry is also present for the undoped compound, along with a weak background optical conductivity that gradually rises to the maximum at 550 meV (peak α that we will discuss below). For all doped samples a prominent MIR peak is centered at about 0.2 eV (peak I) for $y = 0.1$, which redshifts upon increasing the doping. This feature is commonly observed in doped Mott insulators, in particular the high-T_c cuprates, and is associated to the dressing of the charge carriers by dynamical degrees of freedom of the system [15,16]. The exact nature of these degrees of freedom is difficult to determine unambiguously; theoretical interpretations include phonons, fluctuations of spin, charge, and loop current, and combinations thereof [17–21].

To identify the structures in the optical spectra and obtain the parameters for characterizing the electronic structure (Table III) we compare the experimental data with a tight-binding calculation of the optical conductivity of the undoped material (Fig. 3, see Appendix B for details of the calculation). The orange curve (model A) corresponds to the parameters used in Ref. [6] to fit the ARPES data. To obtain a better match of peak α we repeated the calculation with a different set of parameters (dark-khaki curve, model B) taking into account

TABLE III. Parameter values used for the calculations of the optical conductivity.

Model	Doping	t_0 eV	Δ_t eV	ϵ_{xy} eV	λ eV	U eV	J eV
A	0	0.23	0.15	−1.5	0.57	2.0	0
A′	0.1	0.35	0.15	−1.5	0.57	0	0
B	0	0.35	0.15	−1.5	0.67	3.1	0.7
B′	0.1	0.35	0.15	−1.5	0.67	0	0

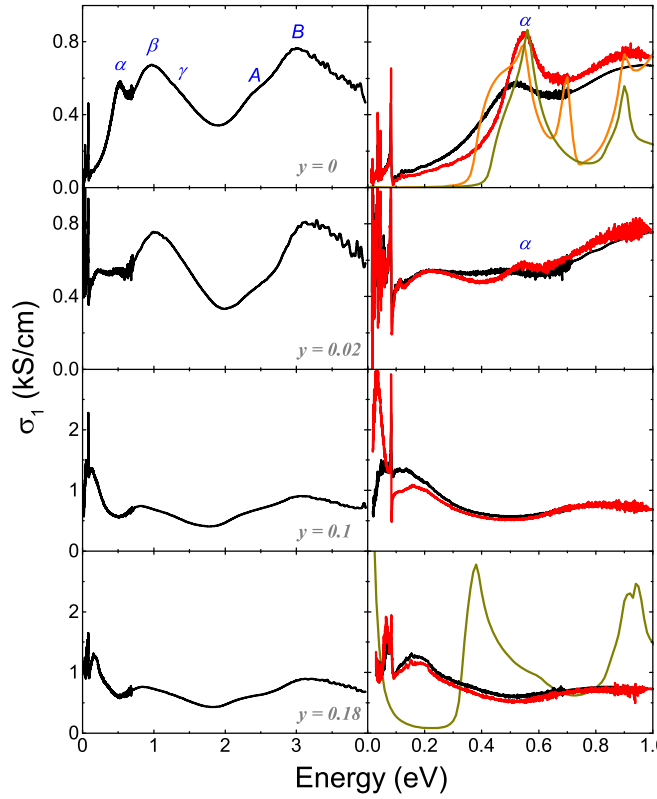

FIG. 3. Left: doping dependence of optical conductivity in the whole measured range. Right: temperature and doping dependence of the real part of optical conductivity below 1 eV. The spectral features are labeled according to Ref. [22]. Tight-binding calculations for the undoped material at 30 K using the parameters A (same parameters as Ref. [6]) and B (best fit to the optical data) of Table III of Appendix B are shown as orange (A) and dark khaki (B, best fit). The result of model A (B) has been scaled down by a factor 5 (2.5) to match the vertical range of the data shown. The dark-khaki curve for $y = 0.18$ was calculated with the same band parameters as the dark-khaki curve of the top panel (parameter set B) but the self-consistent solution of the band structure gives a smaller Hubbard gap due to the electron doping.

the exchange interaction within the Ir-5d shell [23]. Peak α at 0.55 eV corresponds to the transition from the lower to the upper Hubbard $j = 1/2$ band (LHB to UHB) and peak β at 1 eV to transitions from the fully occupied $j = 3/2$ band to the UHB, which confirms the generally agreed assignment of these peaks [22,24–27].

III. DISCUSSION OF THE RESULTS

The influence of raising the temperature is to deplete the intensity of peak α. At least two factors contribute to the observed temperature dependence: loss of short range antiferromagnetic correlations [28] and change of the Ir-O-Ir bond angles [22]. Infrared near-field images (see Appendix A) of the $y = 0.02$ sample clearly indicate insulating islands of various length scales embedded in a metallic bath. STM studies of the doped material have indicated nanoscale regions where the Mott gap is fully intact, coexisting with metallic regions [29]. The presence of the α feature is a natural consequence, which

indeed we observe for the $y = 0.02$ doped sample (see Fig. 3). The observed oscillator strength in Fig. 1 corresponds to about 15% of insulating inclusions. In a recent study Seo *et al.* [27] measured the optical spectra of crystals of $Sr_{2-y}La_yIrO_4$ and obtained optical spectra for $y \sim 0.13$ very similar to the $y = 0.02$ data of the present study and much less spectral weight than for the $y = 0.1$ sample reported here in the region below 0.5 eV. We speculate that these differences may arise from differences in effective electron doping associated with the oxygen stoichiometry. In particular if there is excess oxygen in the samples, part of the electrons donated by the lanthanum atoms would become trapped by oxygen acceptor states. The data for $y = 0.1$ and $y = 0.18$ shown in Fig. 1 represent in this respect a considerably higher charge carrier density than recently reported results. The doping dependent suppression of α has also been observed in epitaxial thin films [30]. The disappearance of peak α for $y > 0.02$ signals the collapse of the Mott gap. In comparison, in the hole-doped cuprates the 2 eV charge transfer gap vanishes at a much higher carrier concentration of 0.1 holes per Cu atom [31].

For the doping dependence of the low energy spectral weight we use the parameter

$$K = \frac{d_c}{4\pi e^2} \sum_j (\hbar\omega_{p,j})^2. \tag{1}$$

Here d_c is the interlayer spacing (i.e., $d_c = c/4 = 0.645$ nm), and the plasma frequencies $\omega_{p,j}$ are obtained from the Drude-Lorentz decomposition as detailed in Appendix A. In the following discussion we will use the data obtained at 9 K. The spectral weight of the zero-energy mode, K^*, is obtained by restricting the aforementioned oscillator sum to the Drude ($j = 0$) peak. This quantity, having units of energy, corresponds to ϵ_F/π for a 2D free electron gas and to $-\epsilon_{\rm kin}/2$ for a single tight-binding band in 2D. The doping dependence displayed in Fig. 4 (bottom panel) follows approximately the linear relation $K^* \approx K_0 y$ where y is the electron count per Ir atom, as expected for doping the Mott-insulating phase. In the present material $K_0 \approx 100$ meV. In comparison, for the hole doped cuprates $K_0 \approx 500$ meV [32], indicating five times lower spectral weight per quasiparticle than in the cuprates. In the same figure we compare this to the spectral weight expected from band-structure calculations. The calculated doping dependence without Hubbard interaction (medium-blue and forest-green curves) is very far from our experimental data. In fact these data approximate more closely the behavior expected for a doped Mott insulator using the Hartree Fock approximation (dark-khaki and orange curves). Despite this reasonably good match these calculations did not reproduce the rapid collapse of the Mott gap at low doping that we observe experimentally, as illustrated in the lower right panel of Fig. 3.

We now turn to the combined *free and bound* intraband spectral weight obtained by restricting the expression for K to the oscillators below 0.5 eV. This spectral weight (Fig. 4, bottom panel) shows a steep rise from the parent compound to the $y = 0.02$ doping, which corresponds to a rapid transfer of high energy to free charge spectral weight, followed by a plateau. Such a behavior is also observed in the cuprates [31,33]. The effective electron number can be calculated from

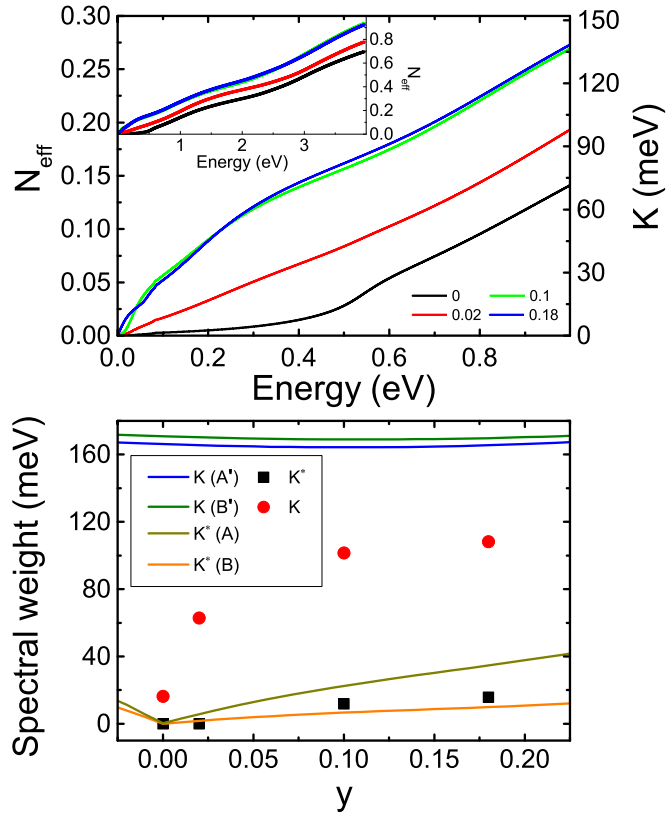

FIG. 4. Top: Effective electron number per Ir atom as a function of energy for different dopings. Bottom: Doping dependence of the coherent (K^*, black squares) and total (K, red circles) free carrier spectral weight. Calculated values are shown for the band parameters reported in Table III.

the optical conductivity using the relation:

$$N_{\rm eff}(\omega) = \frac{2m_e V_u}{\pi e^2} \int_0^{\omega} \sigma_1(\omega')d\omega', \tag{2}$$

where m_e is the free electron mass and $V_u = 97.1$ Å^3 is the volume of one formula unit, and $N_{\rm eff}(\infty)$ corresponds to the total number of electrons per formula unit. Limiting the integral to the zero-energy mode provides $K^* m_e V_u/(d_c\hbar^2)$. $N_{\rm eff}(\omega)$ at $T = 9$ K is displayed in Fig. 4. The change of slope of the parent compound at 0.55 eV clearly shows the onset of the Mott gap. For the two highest dopings, $N_{\rm eff}(\omega)$ rises steeply from zero energy due to the zero energy mode. For all samples the contribution of optical phonons is negligible as compared to the electronic spectral weight. The effect of doping is to deposit spectral weight below 0.55 eV, while the spectral weight from 0.55 to 4 eV is only weakly affected. Doping with $y = 0.02$, $y = 0.10$, and $y = 0.18$ electrons adds amounts $\Delta N_{\rm eff} = 0.045, 0.125$, and 0.125, respectively, in the range below 0.55 eV. Above 0.55 eV the slope of $N_{\rm eff}(\omega)$ is approximately the same for all doping levels, indicating that the effect of doping only weakly affects the optical spectra from 0.55 to 4 eV. Hence we see that for $y = 0.02$ and $y = 0.10$ *more* low energy spectral weight is added than the number of electrons doped. However, the f-sum rule implies that for $\omega \to \infty$ the distance between the $N_{\rm eff}$ curves corresponds to the difference in electron count. The implication is that the extra

spectral weight below 0.55 eV is transferred from energies above 4 eV, an effect generally understood to result from strong electron correlations. Indeed the effect of switching on U and J is to transfer spectral weight from the zero-energy mode to higher energies. Integrating the optical conductivity to energies well above the Hubbard U should recover most of the transferred spectral weight. We therefore expect K and $N_{\rm eff}(\omega \sim U)$ to exhibit the doping trend of the band model with $U = J = 0$, which is indeed almost doping independent as shown by the forest-blue and medium-green curves in the lower panel of Fig. 4.

Implications for the state of matter

The midinfrared feature I at 0.2 eV (Fig. 1) is present for all doping concentrations, and its intensity tracks the doping concentration. Similar features and doping dependence are common in doped Mott insulators (for a summary see Sec. III C of Ref. [34]) and signal the incoherent side bands of the Drude peak due to coupling of the conduction electrons to dynamical degrees of freedom such as phonons, magnons, and combinations thereof. In the cuprates the midinfrared band has been associated to the pseudogap observed with other techniques [34]. Recent dynamical mean field calculations of doped Sr_2IrO_4 show that the gap at the $(\pi,0)$ point persists at finite doping as a finite-size—but much smaller—pseudogap [35]. Seeing a pronounced feature like this is typically associated to the regime of low density and strong coupling, resulting in polaronic charge carriers due to coupling to vibrational degrees of freedom. The resulting charge carrier effective masses are typically two to four times the bare band mass. The possibility of a polaronic nature of the charge carriers in Sr_2IrO_4 has been previously proposed on the basis of ARPES [36] and optics [25]. The doping dependence of the SCM shows a similar wiping out at high carrier concentrations as observed in $Nd_{2-x}Ce_xCuO_4$ [37]. An interesting explanation of this doping dependence [38] interprets the SCM observed in this electron doped cuprate as an internal mode of the polaron, which should become unstable for large concentration due to dipole-dipole interactions. This in turn leads to a rapid doping dependent softening of this internal mode. This interpretation finds additional support from the observation of a strong Fano asymmetry of the phonons overlapping with peak S in our measurements. Since both electron-phonon coupling and Mott physics appear to be important in the iridates, and moreover these materials are doped by chemical substitution of donor atoms, it is of interest to consider the effects of doping a Mott insulating state by chemical substitution. In a recent theoretical discussion of $R_{1-x}Ca_xVO_3$ the effects of disordered charged defects on the spectral function in the Mott insulating regime [39] were shown to trigger small spin-orbital polarons, with their internal kinetic energy responsible for the opening of the soft defect states gap inside the Mott gap. Breaking of translation invariance is a natural consequence of the disorder potential due to the randomly substituted La^{3+} donor atoms. The fact that the SCM has a finite energy requires pinning of the translational motion of the collective charge motion, without which the SCM would show up as a zero-energy mode.

All these arguments require that the nature of the charge response is manifestly collective, i.e., it is necessary to consider the motion of the electronic liquid as a whole as opposed to that of single electrons. In a number of recent papers a hydrodynamic instead of corpuscular approach has been explored for the transport [40] and optical [41] properties of strongly interacting matter. Recently a theoretical description of the collective hydrodynamic motion of an incommensurate charge density wave state lead to the prediction of optical spectra with a SCM very similar to those shown in Fig. 1, together with T-linear DC resistivity at high enough temperature. The peak structure in the optical spectra derives in this case from finite energy oscillations of a charge density wave phason pinned by broken translation invariance of the system [42,43]. Experimentally for the $y = 0.1$ and $y = 0.18$ samples the pinned collective state appears shunted by a finite DC resistivity, preventing the resistivity from diverging for $T \to 0$, which is also in good agreement with the model of Refs. [42,43]. It is possible that on a microscopic level this metallic conducting component is characterized by fermions with a Fermi surface of which a finite fraction remains ungapped.

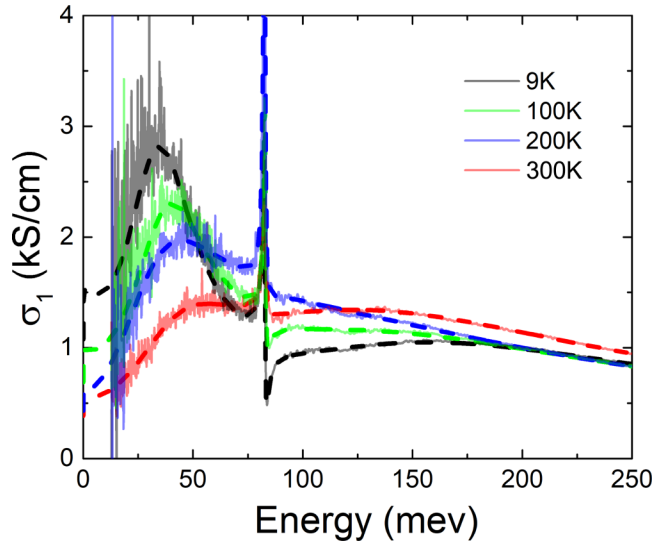

FIG. 5. Zoom of the optical conductivity in the SCM region of sample $y = 0.1$.

If we now take a look at the temperature dependence of the SCM, shown in Fig. 5 for the $y = 0.1$ sample where the SCM is the most clearly manifested, we notice two important trends in the temperature dependence: Increasing temperature causes both a blueshift and a loss of spectral weight of the SCM. This lost SCM spectral weight is transferred to the spectral range above 0.1 eV and almost fully recovered below 0.25 eV. Since Lorenzana did not explicitly work out the temperature dependence [38], a direct comparison to Fig. 5 cannot be made.

In the context of the model of Delacretaz *et al.* the strongest temperature dependent blueshift is expected in a quantum critical state of matter [42,43], in which case $\omega_0 \propto k_B T/\hbar$. Our experimental temperature dependence has the same sign, but for $T \to 0$ the SCM position saturates at 35 meV instead of converging to zero. This saturation at low temperatures would imply that quantum criticality is not realized for the doping values in this study. The emerging picture in the context of the model of Delacretaz *et al.* is that of a state of matter characterized by two components existing in parallel: (i) A

charge density wave which is pinned to the disorder potential but can be excited at finite energy giving rise to a SCM. (ii) An interacting electron liquid which is partially ungapped at the Fermi surface.

On the basis of our present data we cannot fully rule out the polaronic interpretation of Lorenzana [38] or the bad metal interpretation of Delacretaz *et al.* [42,43]. Moreover, both electron-electron interactions [16] and electron-phonon interactions [44] give rise to significant mass renormalization in low doped transition metals, making it difficult to separate these effects. On the other hand there is an important qualitative difference: The polaronic interpretation [38] does not require disorder for the SCM to appear at nonzero frequencies, whereas in the work Delacretaz *et al.* weak disorder is a requirement for the CDW to appear at nonzero energy. Since in practice weak disorder in materials is a sensitive parameter of preparation conditions, the latter interpretation would then imply considerable sample-to-sample differences of the SCM. A systematic study of this question will become possible when highly doped Sr_2IrO_4 crystals can be routinely produced.

IV. CONCLUSIONS

We observed in the optical conductivity of doped $Sr_{2-y}La_yIrO_4$ a rapid erosion of the 0.55 eV Mott gap when the material is electron doped by chemical substitution of La on the Sr site. Doping introduces various features below 0.55 eV, in particular a zero-energy mode, an SCM in the range 35–60 meV and a midinfrared band at 0.2 eV. The doping evolution of these features indicates that the material remains strongly correlated for all doping values studied up to the maximum doping obtained, $y = 0.18$. We also measure a low temperature upturn in the DC resistivity, even at this high doping, whereas the high temperature dependence is approximately T linear. The 0.2 eV peak is similar to many other doped Mott insulators, which for this reason we attribute to strong coupling of the electrons to vibrational and spin degrees of freedom. The SCM, its energy and dependence on doping and temperature, as well as the T-linear DC resistivity at high T and the upturn at low T can be understood as a charge density wave pinned to impurities, parallel shunted by a metallically conducting component.

ACKNOWLEDGMENTS

We gratefully acknowledge discussions with C. Berthod and T. Giamarchi. This project was supported by the Swiss National Science Foundation (projects 200021-153405 and 200021-162628.).

K.W. and N.B. contributed equally to this work.

APPENDIX A: EXPERIMENTAL METHODS

1. Crystal growth and characterization

Single crystals of $Sr_{2-y}La_yIrO_4$ were flux grown by heating a mixture of off-stoichiometric quantities of IrO_2, La_2O_3, and $SrCO_3$ in an anhydrous $SrCl_3$ flux to 1245 °C for 12 hours and cooling the mixture at a rate of ∼8 °C/hour to 1100 °C before quenching to room temperature. The typical sample size that was obtained by this method is about 200 μm to 600 μm. The La concentration was determined by wavelength dispersive spectroscopy (WDS). We used the van der Pauw method to measure the DC resistivity shown in Fig. 2. For the $y = 0.1$ and $y = 0.18$ samples we also measured the Hall coefficient, from which we calculated effective carrier density and the mobility, presented in Fig. 6 for the purpose of characterization and comparison to samples used by different research groups. The mobility (right-hand panels of Fig. 6) becomes strongly suppressed when the temperature drops below 50 K (100 K) for the $y = 0.1$ ($y = 0.18$) sample. The effective densities obtained from the Hall coefficient are smaller than the nominal values La concentrations ($n = 1.03 \times 10^{21}$ cm^{-3} for the $y = 0.1$ sample and $n = 1.85 \times 10^{21}$ cm^{-3} for the $y = 0.18$ sample). The strong temperature dependence signals that the current is carried by two or more types of charge carriers with different mobilities and prohibits obtaining the carrier density unambiguously from the Hall data. We also measured the Fermi-volume area of samples of the same batch using angle resolved photoelectron spectroscopy (ARPES) [6] which, by virtue of the Luttinger sum rule, provides the carrier density. The WDS and ARPES numbers are summarized in Table I. For the discussion in this paper we will label the samples by the WDS values of y in the first column of this table.

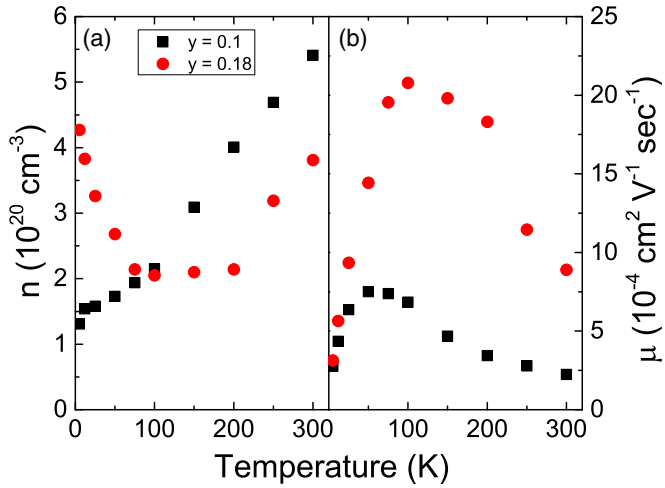

FIG. 6. Temperature dependence of Hall density (a) and Hall mobility (b) for the $y = 0.1$ and the $y = 0.18$ sample.

2. Determination of the dielectric function and the optical conductivity

Prior to the optical measurements all samples were cleaved *ex situ*, resulting in clean and mirrorlike sample surfaces. We measured the near normal reflectivity from 12.5 meV to 50 meV with a Fourier transform spectrometer combined with a UHV flow cryostat, using *in situ* gold evaporation for calibrating the signal. The reflectance from 50 meV to 1.25 eV was measured with an infrared microscope and a flow cryostat coupled to a Fourier spectrometer, using for calibration an *ex situ* deposited gold layer covering half of the sample surface. In the energy range from 0.5 eV to 4 eV we measured the complex dielectric function using ellipsometry of the ab plane of our samples at an incident angle 65° relative to the normal. Following Aspnes this geometry provides the a-axis tensor element of the dielectric function with a

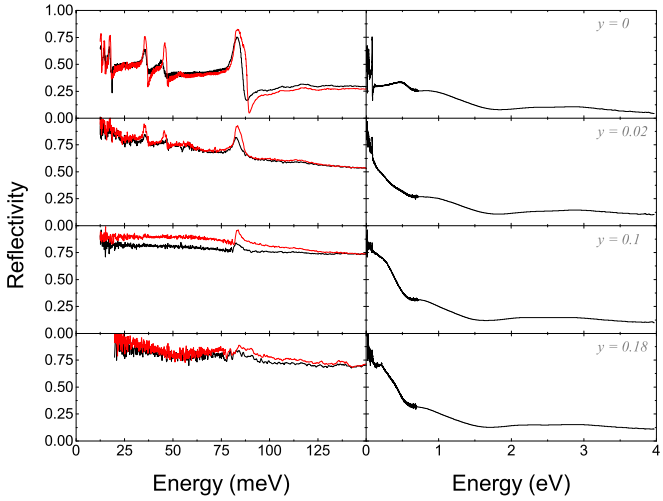

FIG. 7. Reflectivity spectra at 4 K and 300 K for different doping levels. Left panel shows an expanded scale from 0 to 150 meV to highlight the range of the optical phonons. At 0.7 eV the reflectance and ellipsometry data were merged. For the latter only 300 K data could be measured, the whole measured data indicated in the right panel. These data were used for the Kramers-Kronig analysis at all other temperatures using the method detailed in this section.

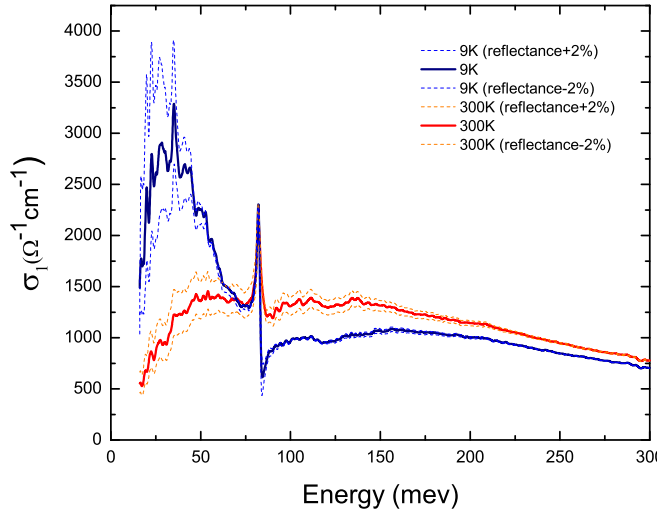

FIG. 8. Comparison for the $y = 0.1$ sample of the Kramers-Kronig output for the optical conductivity with and without an overall vertical shift of the reflectance spectra by ±2%. Since our cryostat design with integrated gold evaporator (used for signal calibration) does not involve any mechanical motion of the sample when comparing sample and reference, the systematic error is in fact below 0.5%.

small c-axis contribution [45]. Correction for this contribution makes negligible difference in the present case [26]. To obtain sufficient signal-to-noise ratio ellipsometry was performed at room temperature, without cryostat. Since the temperature dependence in this energy range is very weak, we use the room temperature data for the Kramers-Kronig analysis of the infrared data at all temperatures.

The following method was used to obtain the optical conductivity:

(i) From 0.5 to 4 eV the complex $\epsilon(\omega) = \epsilon_1(\omega) + i\epsilon_2(\omega)$ was used to calculate complex reflectivity coefficient $|r|e^{i\phi}$ using Fresnel's equation. The reflectivity spectra $R(\omega) = |r(\omega)|^2$ from 12 meV to 4 eV, combining reflectivity and ellipsometric data, are shown for two temperatures in Fig. 7.

(ii) Fitting the infrared absolute reflectance $|r(\omega)|$ and visible range complex reflectivity $r(\omega)$ simultaneously with a Drude-Lorentz expansion of $\epsilon(\omega)$ provides extrapolations of $|r(\omega)|$ in the ranges {0; 12 meV} and {4 eV; ∞}.

(iii) Application of the Kramers-Kronig relation to $|r(\omega)|$ in the range {0; ∞} provides the phase of the infrared reflectance.

(iv) Inversion of the Fresnel equation than gives a reliable determination of the complex dielectric function $\epsilon(\omega)$ and the optical conductivity $4\pi\sigma_1(\omega) = \omega\epsilon_2(\omega)$ in the entire range of the experimental data.

(v) The optical conductivity spectra were binned in 0.3 meV intervals as compared to 0.04 meV of the original reflectivity data shown in Fig. 7.

(vi) In Fig. 8 we compare the Kramers-Kronig output without and with an overall offset of the reflectance spectra by 2%. The results demonstrate that the shape and position of the SCM are not significantly affected by this level of uncertainty. Overall, the optical conductivity at low frequencies approaches the zero frequency limit defined by the DC conductivity of this sample. We have also checked that different extrapolation methods between 0 and 12 meV give the same optical conductivity spectra above 12 meV.

3. Multioscillator fit

To characterize the free and bound charge contributions to the optical conductivity, we fitted the experimental data to the following set of expressions for the dielectric function, using the Fresnel equations for the reflectivity and ellipsometry coefficients:

$$\epsilon(\omega) = \epsilon_\infty + \frac{4\pi}{i\omega}\sigma(\omega). \tag{A1}$$

The parameter ϵ_∞ subsumes all bound charge contributions corresponding to interband transitions above the fitted energy range (i.e., 4 eV), and

$$\sigma(\omega) = \frac{\omega_p^2}{4\pi}\frac{\tau}{1 - i\omega\tau} + \sum_j \frac{S_j\omega_j^2}{4\pi}\frac{\omega + i\omega_j\tan\theta_j}{\gamma_j\omega + i\left(\omega_j^2 - \omega^2\right)}. \tag{A2}$$

Here the first term describes the Drude component, and the sum over j describes all bound charge contributions, including the optical phonons. The parameter θ_j describes the Fano asymmetry of the jth optical phonon. All other oscillators could be fitted assuming a Lorentzian profile. The fitting parameters for the phonons of the $y = 0$ sample are reported in Table II. In Fig. 9 the optical conductivity of the 10% doped sample at 9 K (black curve in the top panel) is shown together with the Drude-Lorentz fit (red dashed line in the top panel). Fits of similar quality were obtained for all other dopings. The middle panel shows the spectral weight of the Drude component for the highest doped samples, and the bottom panel shows the SCM for all doped samples. Note that for the $y = 0$ and $y = 0.02$ samples the Drude weight is negligible and that there is no SCM for the $y = 0$ sample.

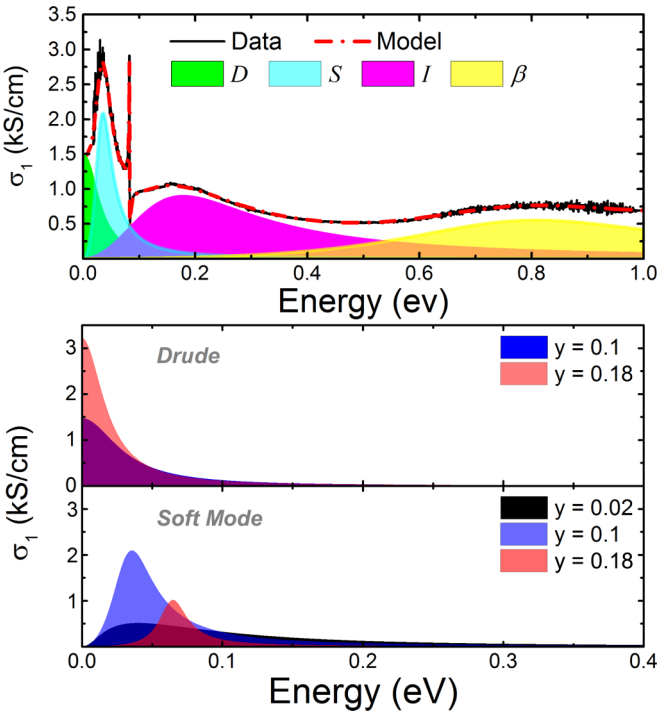

FIG. 9. Top: The solid black curve is the real part of the optical conductivity $\sigma_1(\omega)$ at 9 K below 1 eV. The Drude-Lorentz fit is indicated by the dashed red line. The color coded shaded areas correspond to the Drude (green) and Lorentz (all other colors) oscillators. Bottom: Drude (top panel) Lorentz (bottom panel) decomposition below 0.4 eV of the doped samples.

4. AFM and near-field optical microscopy

Scattering-type scanning near-field optical microscopy allows imaging of surface optical properties. Here we used the probing energy of 110 meV (~11 μm wavelength) and the resolution scale is 25 nm. We present images of atomic force topography and the locally back-scattered near-field signal amplitude at room temperature, shown in panels (a) and (b) of Fig. 10, respectively. Metallic regions where the dc conductivity is high and the real part of the dielectric function is negative at the probing energy yield high nano-IR signals [46]. The red color represents metallic domains and dark blue represents insulating domains. For the $y = 0.02$ doped sample the images demonstrate electronic heterogeneity with insulating islands of 0.2 to 1 μm size in a metallic background. This corroborates the observation of a remnant of the α peak in Fig. 3 for this doping level. Zooming in on the metallic region displays additional heterogeneity, showing insulating islands on the 50–100 nm scale. The microscopic origin of heterogeneity is most likely originating in local fluctuations of the La spatial distribution, which already present when distributing the La ions randomly, but may be accentuated further due to clustering. These observations confirm the observations with STM on the nanometer scale [29]. A very important point for the present study is the high level of homogeneity of the $y = 0.1$ sample on a length scale above 25 nm. This is also the case for the $y = 0.18$ sample (not shown here).

APPENDIX B: SELF-CONSISTENT HARTREE CALCULATIONS OF THE OPTICAL PROPERTIES

We calculated the electronic structure in the subset of t_{2g} states using a tight-binding formalism. We used the following tight-binding Hamiltonian including the Coulomb and exchange interactions within the t_{2g} orbitals [23,47–51].

$$\hat{H} = \sum_{\langle ij\rangle\alpha\beta\sigma} t_{ij}^{\alpha\beta}\hat{c}_{i\alpha\sigma}^{\dagger}\hat{c}_{j\beta\sigma} + \sum_{i}\left(\Delta_t \hat{c}_{id_{xy}\sigma}^{\dagger}\hat{c}_{id_{xy}\sigma} + \lambda\hat{\vec{L}}_i\cdot\hat{\vec{S}}_i\right)$$
$$+ U\sum_{m}\hat{n}_{m\uparrow}\hat{n}_{m\downarrow} + \sum_{m>m',\sigma}\left[(U-2J)\hat{n}_{m',\sigma}\hat{n}_{m,\underline{\sigma}}\right.$$
$$+ (U-3J)\hat{n}_{m'\sigma}\hat{n}_{m\sigma} - J\hat{c}_{im\sigma}^{\dagger}\hat{c}_{im\underline{\sigma}}\hat{c}_{im'\underline{\sigma}}^{\dagger}\hat{c}_{im'\sigma}$$
$$\left. - J\hat{c}_{im\sigma}^{\dagger}\hat{c}_{im\underline{\sigma}}^{\dagger}\hat{c}_{im'\underline{\sigma}}\hat{c}_{im'\sigma}\right] \quad \text{(B1)}$$

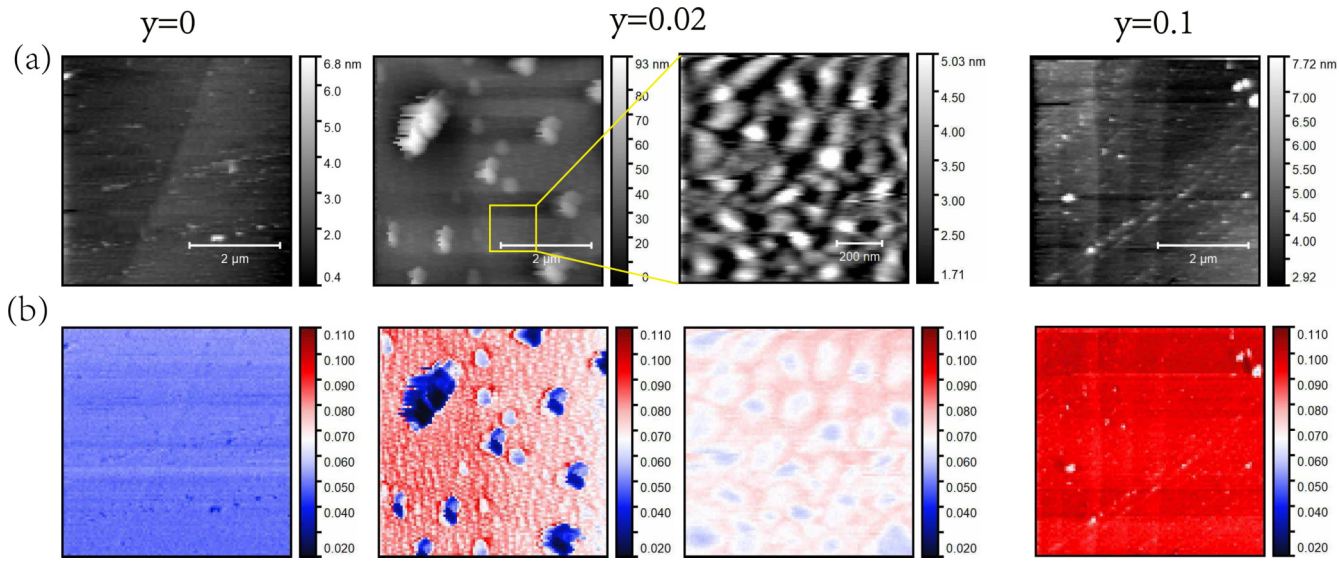

FIG. 10. Atomic force microscopy (a) and near-field infrared optics (b) for a pristine sample and two samples with different doping levels.

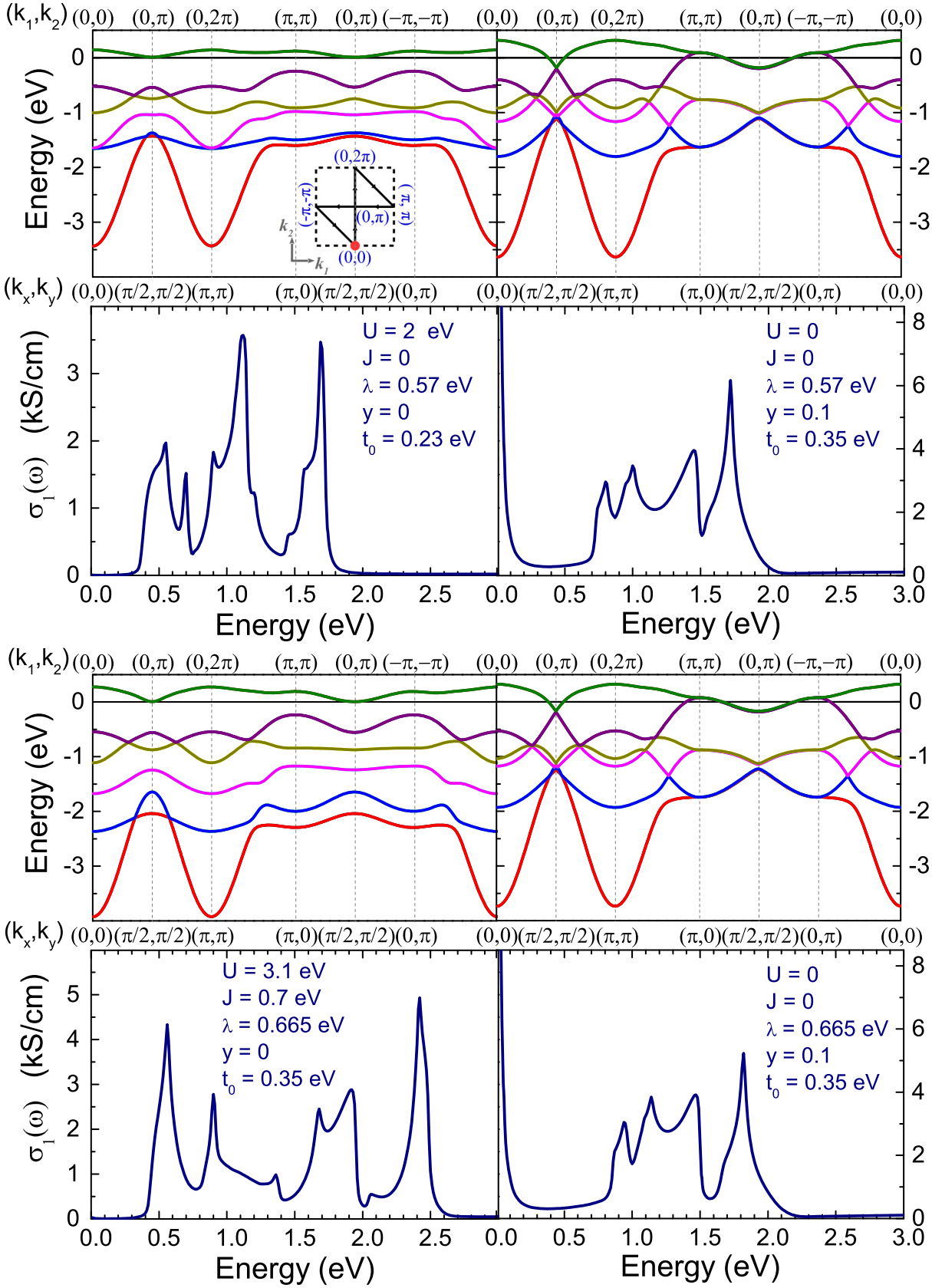

FIG. 11. Top panels: Band structure (top) and optical conductivity corresponding to model A (left) and A′ (right) of Table III. Different colors are used to distinguish the different bands more easily, but they have no additional meaning. Bottom panels: Band structure (top) and optical conductivity corresponding to model B (left) and B′ (right) of Table III. Labels (k_1,k_2) along the top refer to the actual $\sqrt{2} \times \sqrt{2}$ unit cell in two dimensions containing 2 Ir atoms. Labels (k_x,k_y) along the bottom refer to the undistorted unit cell in two dimensions containing 1 Ir atom and with k_x, k_y along the Ir-O bond direction.

The band structure was calculated treating the interaction terms in the self-consistent Hartree-Fock approximation. The total basis consists of three t_{2g} orbitals with two spin values for each of the two sites. The result is a 12×12 Hamiltonian, which splits up in two disjoint 6×6 blocks on the bases $\{d_{A,xy,\sigma}, d_{A,yz,\underline{\sigma}}, d_{A,zx,\underline{\sigma}}, d_{B,xy,\sigma}, d_{B,yz,\underline{\sigma}}, d_{B,zx,\underline{\sigma}}\}$. For each of the two 6×6 blocks one obtains

$$H(k) = \begin{bmatrix} h_{xy} & \frac{\lambda}{2} & \frac{-i\lambda}{2} & -4lt_1 & 0 & 0 \\ \frac{\lambda}{2} & 0 & \frac{-i\lambda}{2} & 0 & -2lt_2 & 0 \\ \frac{i\lambda}{2} & \frac{i\lambda}{2} & 0 & 0 & 0 & -2lt_3 \\ -4l^*t_1 & 0 & 0 & h_{xy} & \frac{\lambda}{2} & \frac{-i\lambda}{2} \\ 0 & -2l^*t_2 & 0 & \frac{\lambda}{2} & 0 & \frac{-i\lambda}{2} \\ 0 & 0 & -2l^*t_3 & \frac{i\lambda}{2} & \frac{i\lambda}{2} & 0 \end{bmatrix} + \begin{bmatrix} V^H_{A,xy,\sigma} & 0 & 0 & 0 & 0 & 0 \\ 0 & V^H_{A,yz,\underline{\sigma}} & 0 & 0 & 0 & 0 \\ 0 & 0 & V^H_{A,zx,\underline{\sigma}} & 0 & 0 & 0 \\ 0 & 0 & 0 & V^H_{B,xy,\sigma} & 0 & 0 \\ 0 & 0 & 0 & 0 & V^H_{B,yz,\underline{\sigma}} & 0 \\ 0 & 0 & 0 & 0 & 0 & V^H_{B,zx,\underline{\sigma}} \end{bmatrix},$$

where

$$\begin{aligned} h_{xy} &= \Delta_t + \epsilon_{xy}\left[\cos\left(\frac{k_1}{2}\right)\cos\left(\frac{k_2}{2}\right)\right]^2 \\ t_1 &= t_0 \cos\left(\frac{k_1}{2}\right)\cos\left(\frac{k_2}{2}\right) \qquad t_2 = t_0 \cos\left(\frac{k_1+k_2}{2}\right) \\ t_3 &= t_0 \cos\left(\frac{k_1-k_2}{2}\right) \qquad\qquad l = \exp\left(-i\frac{k_1+k_2}{2}\right) \\ V^H_{j,xy,\sigma} &= U\langle \hat{n}_{j,xy,\underline{\sigma}}\rangle + (U-2J)\langle \hat{n}_{j,yz,\underline{\sigma}} + \hat{n}_{j,zx,\underline{\sigma}}\rangle + (U-3J)\langle \hat{n}_{j,yz,\sigma} + \hat{n}_{j,zx,\sigma}\rangle etcycl. \end{aligned} \tag{B2}$$

Diagonalization of the Hamiltonian is achieved by a unitary transformation

$$\epsilon_{\vec{k},j} = \sum_{\eta,\mu} u^*_{\eta,j} H_{\eta,\mu} u_{\mu,j}(\vec{k}). \tag{B3}$$

The eigenvalues $\epsilon_{k,j}$ and the unitary transformation matrix $u_{\mu,j}(\vec{k})$ were obtained with the lapack routine ZHEEV for diagonalization of Hermitian matrices. The optical conductivity was calculated from the expression

$$\overleftrightarrow{\sigma}(\omega) = \frac{q_e^2}{\Omega}\sum_{\vec{k},j}^{1'BZ} \vec{v}_{j,j}(\vec{k})\vec{v}_{j,j}(\vec{k})\left(-\frac{\partial f_{\vec{k},j}}{\partial \epsilon_{\vec{k},j}}\right)\frac{i}{\omega + i\delta} + \frac{q_e^2}{\Omega}\sum_{\vec{k},j\neq m}^{1'BZ} \vec{v}_{j,m}(\vec{k})\vec{v}_{m,j}(\vec{k})\frac{f_{\vec{k},j} - f_{\vec{k},m}}{\varepsilon_{\vec{k},m} - \varepsilon_{\vec{k},j}}\frac{i\omega}{\omega(\omega + i\delta) - (\varepsilon_{\vec{k},m} - \varepsilon_{\vec{k},j})^2},$$

where

$$\vec{v}_{j,m}(\vec{k}) = \sum_{\eta,\mu} u^*_{\eta,j}(\vec{k}) u_{\mu,m}(\vec{k})\left[\frac{\partial}{\partial \vec{k}} H_{\eta,\mu}(\vec{k}) + i(\vec{d}_\mu - \vec{d}_\eta) H_{\eta,\mu}(\vec{k})\right] \tag{B4}$$

and $\vec{d}_\mu$ is the center coordinate of the μth Wannier orbital in the unit cell.

Numerical examples are shown in Fig. 11 where the Hartree potential resulting from finite U and J was calculated self-consistently. Convergence was reached after about 20 iterations. The parameter values are summarized in Table III. The parameter sets A ($y = 0$) and A′ ($y = 0.1$) were adopted from Ref. [6] for the sake of comparison with the calculations of the energy-momentum dispersion observed with ARPES. The parameter set B provides the best fit to the experimental data of the undoped parent material (see Fig. 3) and were also used for comparison to the $y = 0.18$ doping shown in the same figure, as well as the calculation of $K^*(y)$ in Fig. 4. The parameter set B′ was used to calculate $K(y)$ in Fig. 4.

From comparing the calculations without and with Hartree potential we see that the undoped insulator has an indirect gap of about 0.2 eV, with a direct gap at the $(\pi,0)$ point of about 0.6 eV. The direct gap is responsible for the α peak. Whereas the interactions cause serious reshuffling of the optical spectrum, the lowest energy peak in the noninteracting case remains at the same position when U and J are switched on. This energy of this peak closely follows the spin-orbit parameter and represents transitions from a band with $j = 3/2$ character to the empty $j = 1/2$ states. Given its relative robustness we attribute this to the β peak in the experimental spectra. We have not been able to adjust parameters such as to fit the entire optical spectrum up to 3 eV. It is conceivable that, as a result of mapping on a limited set of states and in the process of adjusting the low energy part of the spectrum to experimental data, the dispersion at higher energies gets underestimated.

[1] B. Keimer, S. A. Kivelson, M. R. Norman, S. Uchida, and J. Zaanen, From quantum matter to high-temperature superconductivity in copper oxides, Nature (London) **518**, 179 (2015), review article.

[2] F. Wang and T. Senthil, Twisted Hubbard Model for Sr_2IrO_4: Magnetism and Possible High Temperature Superconductivity, Phys. Rev. Lett. **106**, 136402 (2011).

[3] X. Chen, T. Hogan, D. Walkup, W. Zhou, M. Pokharel, M. Yao, W. Tian, T. Z. Ward, Y. Zhao, D. Parshall, C. Opeil, J. W. Lynn, V. Madhavan, and S. D. Wilson, Influence of electron doping on the ground state of $(Sr_{1-x}La_x)_2IrO_4$, Phys. Rev. B **92**, 075125 (2015).

[4] H. Gretarsson, N. H. Sung, J. Porras, J. Bertinshaw, C. Dietl, Jan A. N. Bruin, A. F. Bangura, Y. K. Kim, R. Dinnebier, Jungho Kim, A. Al-Zein, M. Moretti Sala, M. Krisch, M. Le Tacon, B. Keimer, and B. J. Kim, Persistent Paramagnons Deep in the Metallic Phase of $Sr_{2-x}La_xIrO_4$, Phys. Rev. Lett. **117**, 107001 (2016).

[5] X. Chen, J. L. Schmehr, Z. Islam, Z. Porter, E. Zoghlin, K. Finkelstein, J. P. C. Ruff, and S. D. Wilson, Unidirectional spin density wave state in metallic $(Sr_{1-x}La_x)_2IrO_4$, Nat. Commun. **9**, 103 (2018).

[6] A. de la Torre, S. McKeown Walker, F. Y. Bruno, S. Riccó, Z. Wang, I. Gutierrez Lezama, G. Scheerer, G. Giriat, D. Jaccard, C. Berthod, T. K. Kim, M. Hoesch, E. C. Hunter, R. S. Perry, A. Tamai, and F. Baumberger, Collapse of the Mott Gap and Emergence of a Nodal Liquid in Lightly Doped Sr_2IrO_4, Phys. Rev. Lett. **115**, 176402 (2015).

[7] Y. K. Kim, N. H. Sung, J. D. Denlinger, and B. J. Kim, Observation of a d-wave gap in electron-doped Sr_2IrO_4, Nat. Phys. **12**, 37 (2016).

[8] Y. J. Yan, M. Q. Ren, H. C. Xu, B. P. Xie, R. Tao, H. Y. Choi, N. Lee, Y. J. Choi, T. Zhang, and D. L. Feng, Electron-Doped Sr_2IrO_4: An Analogue of Hole-Doped Cuprate Superconductors Demonstrated by Scanning Tunneling Microscopy, Phys. Rev. X **5**, 041018 (2015).

[9] L. Zhao, D. H. Torchinsky, H. Chu, V. Ivanov, R. Lifshitz, R. Flint, T. Qi, G. Cao, and D. Hsieh, Evidence of an odd-parity hidden order in a spin-orbit coupled correlated iridate, Nat. Phys. **12**, 32 (2015).

[10] S. Zhou, K. Jiang, H. Chen, and Z. Wang, Correlation Effects and Hidden Spin-Orbit Entangled Electronic Order in Parent and Electron-Doped Iridates Sr_2IrO_4, Phys. Rev. X **7**, 041018 (2017).

[11] A. B. Kuzmenko, D. van der Marel, F. Carbone, and F. Marsiglio, Model-independent sum rule analysis based on limited-range spectral data, New J. Phys. **9**, 229 (2007).

[12] H. Gretarsson, J. Sauceda, N. H. Sung, M. Höppner, M. Minola, B. J. Kim, B. Keimer, and M. Le Tacon, Raman scattering study of vibrational and magnetic excitations in $Sr_{2-x}La_xIrO_4$, Phys. Rev. B **96**, 115138 (2017).

[13] M. J. Rice, N. O. Lipari, and S. Strässler, Dimerized Organic Linear-Chain Conductors and the Unambiguous Experimental Determination of Electron-Molecular-Vibration Coupling Constants, Phys. Rev. Lett. **39**, 1359 (1977).

[14] A. Damascelli, K. Schulte, D. van der Marel, and A. A. Menovsky, Infrared spectroscopic study of phonons coupled to charge excitations in FeSi, Phys. Rev. B **55**, R4863 (1997).

[15] J. Hwang, T. Timusk, and G. D. Gu, High-transition-temperature superconductivity in the absence of the magnetic-resonance mode, Nature (London) **427**, 714 (2004).

[16] E. van Heumen, E. Muhlethaler, A. B. Kuzmenko, H. Eisaki, W. Meevasana, M. Greven, and D. van der Marel, Optical determination of the relation between the electron-boson coupling function and the critical temperature in high-T_c cuprates, Phys. Rev. B **79**, 184512 (2009).

[17] C. M. Varma, S. Schmitt-Rink, and Elihu Abrahams, Charge transfer excitations and superconductivity in ionic metals, Solid State Commun. **62**, 681 (1987).

[18] C. L. Kane, P. A. Lee, and N. Read, Motion of a single hole in a quantum antiferromagnet, Phys. Rev. B **39**, 6880 (1989).

[19] T. M. Rice and F. C. Zhang, Frequency-dependent conductivity from carriers in Mott insulators, Phys. Rev. B **39**, 815 (1989).

[20] M. Tachiki and S. Takahashi, Pairing interaction mediated by the Cu-O charge-transfer oscillations associated with LO phonons in oxide superconductors and their high-T_c superconductivity, Phys. Rev. B **38**, 218 (1988).

[21] M. Grüeninger, D. van der Marel, A. Damascelli, A. Zibold, H. P. Geserich, A. Erb, M. Kläser, Th. Wolf, T. Nunner, and T. Kopp, Charged magnons and magneto-elastic polarons in the mid-infrared spectrum of $YBa_2Cu_3O_6$, Physica C: Superconductivity **317-318**, 286 (1999).

[22] S. J. Moon, Hosub Jin, W. S. Choi, J. S. Lee, S. S. A. Seo, J. Yu, G. Cao, T. W. Noh, and Y. S. Lee, Temperature dependence of the electronic structure of the $J_{\rm eff} = \frac{1}{2}$ Mott insulator Sr_2IrO_4 studied by optical spectroscopy, Phys. Rev. B **80**, 195110 (2009).

[23] D. van der Marel and G. A. Sawatzky, Electron-electron interaction and localization in d and f transition metals, Phys. Rev. B **37**, 10674 (1988).

[24] B. J. Kim, Hosub Jin, S. J. Moon, J.-Y. Kim, B.-G. Park, C. S. Leem, Jaejun Yu, T. W. Noh, C. Kim, S.-J. Oh, J.-H. Park, V. Durairaj, G. Cao, and E. Rotenberg, Novel $J_{\rm eff} = 1/2$ Mott State Induced by Relativistic Spin-Orbit Coupling in Sr_2IrO_4, Phys. Rev. Lett. **101**, 076402 (2008).

[25] C. H. Sohn, M.-C. Lee, H. J. Park, K. J. Noh, H. K. Yoo, S. J. Moon, K. W. Kim, T. F. Qi, G. Cao, D.-Y. Cho, and T. W. Noh, Orbital-dependent polaron formation in the relativistic Mott insulator Sr_2IrO_4, Phys. Rev. B **90**, 041105 (2014).

[26] D. Pröpper, A. N. Yaresko, M. Höppner, Y. Matiks, Y.-L. Mathis, T. Takayama, A. Matsumoto, H. Takagi, B. Keimer, and A. V. Boris, Optical anisotropy of the $J_{\rm eff} = 1/2$ Mott insulator Sr_2IrO_4, Phys. Rev. B **94**, 035158 (2016).

[27] J. H. Seo, G. H. Ahn, S. J. Song, X. Chen, S. D. Wilson, and S. J. Moon, Infrared probe of pseudogap in electron-doped Sr_2IrO_4, Sci. Rep. **7**, 10494 (2017).

[28] M. Aichhorn, P. Horsch, W. von der Linden, and M. Cuoco, Temperature dependence of optical spectral weights in quarter-filled ladder systems, Phys. Rev. B **65**, 201101 (2002).

[29] I. Battisti, K. M. Bastiaans, V. Fedoseev, A. de la Torre, N. Iliopoulos, A. Tamai, E. C. Hunter, R. S. Perry, J. Zaanen, F. Baumberger, and M. P. Allan, Universality of pseudogap and emergent order in lightly doped Mott insulators, Nat. Phys. **13**, 21 (2016).

[30] J. S. Lee, Y. Krockenberger, K. S. Takahashi, M. Kawasaki, and Y. Tokura, Insulator-metal transition driven by change of doping and spin-orbit interaction in Sr_2IrO_4, Phys. Rev. B **85**, 035101 (2012).

[31] S. Uchida, T. Ido, H. Takagi, T. Arima, Y. Tokura, and S. Tajima, Optical spectra of $La_{2-x}Sr_xCuO_4$: Effect of carrier doping on the electronic structure of the CuO_2 plane, Phys. Rev. B **43**, 7942 (1991).

[32] S. I. Mirzaei, D. Stricker, J. N. Hancock, C. Berthod, A. Georges, E. van Heumen, M. K. Chan, X. Zhao, Y. Li, M. Greven, N. Barisic, and D. van der Marel, Spectroscopic evidence for Fermi

liquid-like energy and temperature dependence of the relaxation rate in the pseudogap phase of the cuprates, Proc. Natl. Acad. Sci. **110**, 5774 (2013).

[33] H. Eskes and G. A. Sawatzky, Single-, triple-, or multiple-band Hubbard models, Phys. Rev. B **44**, 9656 (1991).

[34] D. N. Basov, R. D. Averitt, D. van der Marel, M. Dressel, and K. Haule, Electrodynamics of correlated electron materials, Rev. Mod. Phys. **83**, 471 (2011).

[35] A. Moutenet, A. Georges, and M. Ferrero, Pseudogap and electronic structure of electron-doped Sr_2IrO_4, Phys. Rev. B **97**, 155109 (2018).

[36] P. D. C. King, T. Takayama, A. Tamai, E. Rozbicki, S. McKeown Walker, M. Shi, L. Patthey, R. G. Moore, D. Lu, K. M. Shen, H. Takagi, and F. Baumberger, Spectroscopic indications of polaronic behavior of the strong spin-orbit insulator $Sr_3Ir_2O_7$, Phys. Rev. B **87**, 241106(R) (2013).

[37] S. Lupi, P. Maselli, M. Capizzi, P. Calvani, P. Giura, and P. Roy, Evolution of a Polaron Band through the Phase Diagram of $Nd_{2-x}Ce_xCuO_{4-y}$, Phys. Rev. Lett. **83**, 4852 (1999).

[38] J. Lorenzana, Instability due to long-range Coulomb interaction in a liquid of Feynman polarons, EPL (Europhysics Letters) **53**, 532 (2001).

[39] A. Avella, A. M. Oleś, and P. Horsch, Fingerprints of spin-orbital polarons and of their disorder in the photoemission spectra of doped Mott insulators with orbital degeneracy, Phys. Rev. B **97**, 155104 (2018).

[40] M. Müller, J. Schmalian, and L. Fritz, Graphene: A Nearly Perfect Fluid, Phys. Rev. Lett. **103**, 025301 (2009).

[41] D. Forcella, J. Zaanen, D. Valentinis, and D. van der Marel, Electromagnetic properties of viscous charged fluids, Phys. Rev. B **90**, 035143 (2014).

[42] L. V. Delacrétaz, B. Goutéraux, S. A. Hartnoll, and A. Karlsson, Bad metals from fluctuating density waves, SciPost Phys. **3**, 025 (2017).

[43] L. V. Delacrétaz, B. Goutéraux, S. A. Hartnoll, and A. Karlsson, Theory of hydrodynamic transport in fluctuating electronic charge density wave states, Phys. Rev. B **96**, 195128 (2017).

[44] J. L. M. van Mechelen, D. van der Marel, C. Grimaldi, A. B. Kuzmenko, N. P. Armitage, N. Reyren, H. Hagemann, and I. I. Mazin, Electron-phonon Interaction and charge Carrier Mass Enhancement in $SrTiO_3$, Phys. Rev. Lett. **100**, 226403 (2008).

[45] D. E. Aspnes, Approximate solution of ellipsometric equations for optically biaxial crystals, J. Opt. Soc. Am. **70**, 1275 (1980).

[46] A. S. McLeod, E. van Heumen, J. G. Ramirez, S. Wang, T. Saerbeck, S. Guenon, M. Goldflam, L. Anderegg, P. Kelly, A. Mueller, M. K. Liu, Ivan K. Schuller, and D. N. Basov, Nanotextured phase coexistence in the correlated insulator V_2O_3, Nat. Phys. **13**, 80 (2016).

[47] C. Martins, M. Aichhorn, L. Vaugier, and S. Biermann, Reduced Effective Spin-Orbital Degeneracy and Spin-Orbital Ordering in Paramagnetic Transition-Metal Oxides: Sr_2IrO_4 versus Sr_2RhO_4, Phys. Rev. Lett. **107**, 266404 (2011).

[48] L. de' Medici, J. Mravlje, and A. Georges, Janus-Faced Influence of Hund's Rule Coupling in Strongly Correlated Materials, Phys. Rev. Lett. **107**, 256401 (2011).

[49] R. Arita, J. Kuneš, A. V. Kozhevnikov, A. G. Eguiluz, and M. Imada, *Ab initio* Studies on the Interplay between Spin-Orbit Interaction and Coulomb Correlation in Sr_2IrO_4 and Ba_2IrO_4, Phys. Rev. Lett. **108**, 086403 (2012).

[50] S. Emori, E. Martinez, K.-J. Lee, H.-W. Lee, U. Bauer, S.-M. Ahn, P. Agrawal, D. C. Bono, and G. S. D. Beach, Spin Hall torque magnetometry of Dzyaloshinskii domain walls, Phys. Rev. B **90**, 184427 (2014).

[51] I. V. Solovyev, V. V. Mazurenko, and A. A. Katanin, Validity and limitations of the superexchange model for the magnetic properties of Sr_2IrO_4 and Ba_2IrO_4 mediated by the strong spin-orbit coupling, Phys. Rev. B **92**, 235109 (2015).